Chemical Geology 704 (2026) 123264

Contents lists available at ScienceDirect

Chemical Geology

journal homepage: www.elsevier.com/locate/chemgeo

Research Paper

CO_2 fluxing and carbon assimilation by arc melts during magma–limestone interaction

Frances M. Deegan [a,*], Manfredo Capriolo [b], Valentin R. Troll [a,c], Franz A. Weis [a,d], Sara Callegaro [e,f], Simone Colucci [g], Carmela Freda [h], Valeria Misiti [i], László E. Aradi [j,k,l], Henrik Skogby [d], Herlan Darmawan [m], Harri Geiger [n]

[a] Department of Earth Sciences, Uppsala University, Uppsala, Sweden
[b] School of Geography, Earth and Environmental Sciences, University of Birmingham, Birmingham, United Kingdom
[c] Faculty of Geological Engineering, Universitas Padjajaran, Bandung, Indonesia
[d] Department of Geosciences, Swedish Museum of Natural History, Stockholm, Sweden
[e] Department of Biological, Geological, and Environmental Sciences, University of Bologna, Bologna, Italy
[f] The NJORD Centre, University of Oslo, Oslo, Norway
[g] Istituto Nazionale di Geofisica e Vulcanologia (INGV), sezione Pisa, Italy
[h] European Plate Observing System, European Research Infrastructure Consortium, Rome, Italy
[i] Istituto Nazionale di Geofisica e Vulcanologia (INGV), sezione Roma, Italy
[j] Lithosphere Fluid Research Laboratory, Institute of Geography and Earth Sciences, Eötvös Loránd University, Budapest, Hungary
[k] Department of Geosciences, University of Padua, Padua, Italy
[l] National Institute of Archaeology, Hungarian National Museum, Budapest, Hungary
[m] Department of Physics, Universitas Gadjah Mada, Yogyakarta, Indonesia
[n] Institute of Earth and Environmental Sciences, University of Freiburg, Freiburg, Germany

ARTICLE INFO

Editor: Claudia Romano

Keywords:
Magma–limestone interaction
Limestone assimilation
CO_2
Degassing
Fourier transform infrared spectroscopy (FTIR)
Raman microspectroscopy

ABSTRACT

Reworking of limestone ($CaCO_3$) by magma is an important source of carbon in volcanic arc emissions. However, while it is broadly understood that CO_2 is liberated during magma–limestone interaction, the degassing behaviour of calcite in silicate melts is less well constrained. In this study, we carried out microspectroscopic analysis of volatiles within fluid inclusions and glass (former melt) in the products of short-term experiments simulating limestone assimilation in mafic arc melt (T = 1200 °C, P = 0.5 GPa, runtimes of 0 to 300 s). The experimental products consist of partly to wholly assimilated limestone xenoliths enveloped by CaO-rich silicate glass (reacting melt) that grades into mafic glass (host melt). Micro- to milli-metric sized fluid-filled bubbles permeate the experimental products. This study reveals that limestone assimilation induces extremely fast apparent diffusivity of CO_2 ($D_{CO2} \gtrsim 10^{-7}$ m^2/s) through both the reacting melt and the host melt. Volatile saturation is thus quickly reached, triggering nucleation of bubbles mainly containing $CO_2 \pm CO$, CH_4, N_2, H_2, and H_2O. Crucially, we find that the host melt contains dissolved CO_2 from limestone, despite showing no other compositional evidence for limestone assimilation. Mafic melts in volcanic regions underlain by limestone may therefore mobilise and transport more carbon than previously thought, with implications for eruptive behaviour, volcanic CO_2 inventories, and long-term climate warming.

1. Introduction

Carbon outgassing from the solid Earth helps modulate the planet's long-term climate and habitability (Lee et al., 2019). Subduction zones are central to the global carbon cycle, as they transfer carbon from the mantle and down-going plate to the atmosphere *via* arc volcanoes (Plank and Manning, 2019). Potentially significant additional sources of carbon are sedimentary rocks located in the upper plate that may be intersected by ascending arc magmas (Mason et al., 2017). Carbon from upper crustal sources is especially important at mature continental arcs, which due to accretion of carbonate platforms over time, may contain up to three times the amount of carbon as the oceans and atmosphere (Lee

* Corresponding author.
E-mail address: frances.deegan@geo.uu.se (F.M. Deegan).

https://doi.org/10.1016/j.chemgeo.2026.123264
Received 13 November 2025; Received in revised form 18 January 2026; Accepted 19 January 2026
Available online 20 January 2026

et al., 2019). Continental arcs therefore act as major repositories of carbon in the Earth's crust. At volcano-magmatic systems built upon carbonate successions (*i.e.* on limestone bedrock), carbon can be liberated as a consequence of contact metamorphic decarbonation reactions surrounding magmatic intrusions or due to magmatic assimilation of limestone wallrock and xenoliths (*e.g.*, Troll et al., 2013; Ramos et al., 2020; see Fig. 1).

Limestone assimilation has been recognized at volcanic arcs through studies of xenoliths and skarn rocks (*e.g.*, Gaeta et al., 2009; Di Rocco et al., 2012; Whitley et al., 2019, 2020); volcanic rocks, minerals, inclusions, and gases (*e.g.*, Chadwick et al., 2007; Iacono-Marziano et al., 2009; Dallai et al., 2011; Troll et al., 2012, 2013; Borisova et al., 2013; Gozzi et al., 2014); and magmatic intrusions emplaced into limestone bedrock (*e.g.*, Barnes et al., 2005; Ramos et al., 2020; Morris and Canil, 2022). Complementary to these are high pressure and temperature experimental investigations and numerical models, which have provided crucial insight into the mechanisms and rates of magma–limestone interaction (*e.g.*, Iacono Marziano et al., 2007, 2008; Freda et al., 2008, 2010; Deegan et al., 2010; Mollo et al., 2010; Jolis et al., 2013; Carter and Dasgupta, 2015, 2016, 2018; Lustrino et al., 2022; Colucci et al., 2024). All of the aforementioned studies underscore that a key characteristic of limestone assimilation is breakdown of $CaCO_3$ to liberate CaO and CO_2 into the magmatic environment. These components can profoundly influence the physical properties of silicate melts and increase their volatile load, which may affect eruptive dynamics and promote explosive eruption styles (Freda et al., 2010; Dallai et al., 2011; Blythe et al., 2015; Carr et al., 2018; Knuever et al., 2023). Moreover, the CO_2 released during limestone assimilation can contribute to volcanic carbon fluxing and may have repercussions for estimates of volcanic carbon inventories and long-term climate change (Johnston et al., 2011; Lee et al., 2013; Aiuppa et al., 2017; Mason et al., 2017; Carter and Dasgupta, 2018).

Although limestone assimilation has important implications for volcanic CO_2 fluxes, eruptive dynamics, and long-term climate, it is not always easily recognisable in melt compositions, especially with respect to major and trace element contents of erupted magmas (*e.g.*, Spandler et al., 2012). Assessing the impact of limestone assimilation on volatile production and transport through magmatic systems is further hampered by the paucity of data available for CO_2 solubility, diffusion, and speciation in silicate melts that have interacted with limestone

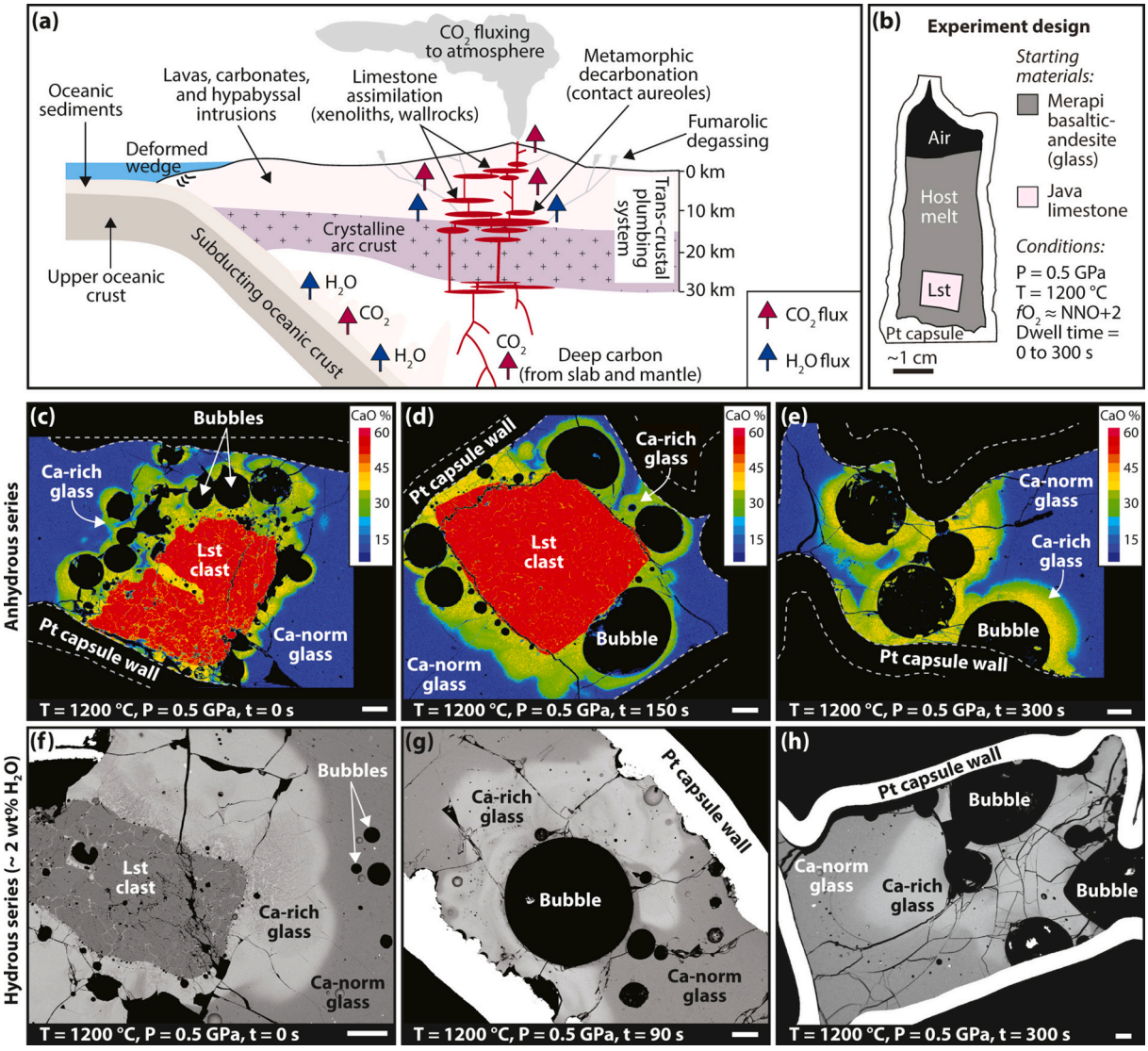

Fig. 1. **(a)** Sketch of an arc magmatic system intersecting limestone. **(b)** Sketch showing the experimental design used in this study. **(c-e)** Calcium element maps of Merapi anhydrous magma–limestone interaction experiments. **(f-h)** Back Scattered Electron (BSE) images of Merapi hydrous magma–limestone interaction experiments. Images in (c) and (d) after Deegan et al. (2023) and in (f) to (h) after Deegan et al. (2010). Abbreviations: Ca-norm, Ca-normal; Lst, limestone. Scale bars are 200 μm unless otherwise stated.

(Baker et al., 2005). Therefore, it can be difficult to determine the significance of limestone assimilation based on magma chemistry and, in turn, the fate of CO_2 liberated from assimilated limestone. As a result, CO_2 fluxing from crustal sources at volcanoes built upon limestone bedrock may be underestimated. In this study, we aim to (i) provide new constraints on CO_2 degassing processes in mafic melts during interaction with limestone and (ii) test whether mafic melts that appear to be uncontaminated by limestone may actually be able to transport limestone-derived CO_2 through magma plumbing systems. To do this, we present quantitative volatile data obtained *via* microspectroscopic analyses of co-existing silicate glasses and fluid inclusions in the products of short-term, high pressure and temperature magma–limestone interaction experiments. By employing the products of experiments conducted with differing runtimes (*i.e.* 0 to 300 s), we trace the progressive effects of limestone assimilation on the generation and mobility of volatiles in mafic melts.

2. Overview of the magma–limestone interaction experiments

The magma–limestone interaction experiments analysed for volatiles in this study were first reported in terms of their textures and major element compositions by Deegan et al. (2010). Subsequent studies employed these experimental products to explore various aspects of magma–limestone interaction, including bubble size distribution, isotope gradients in contaminated glass, and melt mixing (*e.g.,* Blythe et al., 2015; Deegan et al., 2016; Colucci et al., 2024). However, volatile data for the experimental products have thus far been lacking, which has precluded a detailed assessment of the degassing phenomena associated with magma–limestone interaction. Here, we present fully quantitative volatile analyses of glass and bubbles (*i.e.* fluid inclusions) in a number of experiments with differing runtimes from the original work of Deegan et al. (2010). We combine our new volatile data with thermodynamically constrained CO_2 solubility and diffusion modelling, to provide robust insights on degassing processes during limestone assimilation by mafic arc melts.

The magma–limestone interaction experiments of Deegan et al. (2010) were designed to reproduce short-term entrainment of limestone xenoliths in anhydrous to hydrous (*ca.* 2 wt% H_2O) mafic arc melts. Since the experiments captured snapshots of the dynamic conditions present at the onset of magma–limestone interaction, they can be considered "kinetic" experiments (see also Deegan et al., 2022). Starting materials were sourced from Mt. Merapi (Central Java, Indonesia), an emblematic and well-studied limestone-intersecting arc volcano located in the Sunda arc, Indonesia (for a review see Deegan et al., 2023; Troll and Deegan, 2023). The experimental charges consisted of 3 mm outer diameter platinum capsules each containing *ca.* 40 mg pulverized hydrous Merapi basaltic-andesite glass (SiO_2 = 51.8 wt%, CaO = 9.2 wt%) and a *ca.* 10 mg limestone clast comprised of almost pure calcite (SiO_2 = 0.3 wt%, CaO = 56.7 wt%). The charges were pressurized in a ½-inch, end-loaded piston cylinder apparatus at Istituto Nazionale di Geofisica e Vulcanologia (INGV) in Rome, Italy. The charges were pressurized to 0.5 GPa at ambient temperature and then heated at a rate of 200 °C/min to 1180 °C, followed by a rate of 20 °C/min to the target temperature of 1200 °C. Once the target temperature was reached, a timer was set for intervals ranging from 0 to 300 s. The temperature was monitored and maintained using a Type C thermocouple. The type of experimental assembly generated an oxidising melt environment, as expected for arc melts, with fO_2 estimated at NNO +2 (Freda et al., 2008). To end the experiment, isobaric quenching was induced at a rate of 2000 °C/min by shutting off the power source. The experiments were then decompressed slowly. The combination of short runtimes and rapid quench rates enabled the preservation of prograde assimilation textures and melt compositions (preserved as glass) that would be overprinted and therefore lost in longer duration runs (Fig. 1). Phase equilibrium estimates for Merapi magma storage yielded temperatures of 925 to 950 °C, with pre-eruptive recharge magmas thought to possess higher temperatures of up to 1000 °C (Erdmann et al., 2016). By employing a relatively high experimental temperature of 1200 °C, the experiments simulated injection of fresh, hot magma into a limestone-hosted magma reservoir or sill.

Once the experimental runs were completed, the charges were retrieved from the pressure vessel, embedded in epoxy resin, and gently polished until a cross section of the interior was visible. The experimental products were then inspected using scanning electron microscopy (SEM) and electron probe microanalysis (EPMA; Deegan et al., 2010). The experimental products for the most part comprise silicate glass (vitrified melt) and fluid-bearing vesicles (fluid inclusions; Fig. 1). In the shortest experiments (runtime = 0 s), limestone is still visible whilst in the longest experiments (runtime = 300 s), the limestone has completely dissolved into the melt. Many experiments also contain relatively small amounts of microcrystals. The glasses can be subdivided into two varieties based on their major element compositions:

(i) *Ca-normal glass.* Refers to the mafic host glass, which is compositionally similar to the Merapi basaltic-andesite starting material. This glass has SiO_2 and CaO contents of around 51 wt% and 9 wt%, respectively, and shows no evidence of limestone contamination in terms of major elements or $^{87}Sr/^{86}Sr$ ratios.
(ii) *Ca-rich glass* (reacting melt). Refers to silicate glass enriched in CaO compared to both the Ca-normal glass and the starting material. The Ca-rich glass forms a compositional boundary layer at the magma–limestone interface and has a relatively low SiO_2 content of *ca.* 27 to 38 wt% and a high CaO content of *ca.* 27 to 34 wt%. This glass also possesses elevated $^{87}Sr/^{86}Sr$ ratios (up to 0.706532 ± 82 2SE).

Further details concerning the preparation and compositions of the starting materials and the experimental method are provided in the **Supplementary material**.

3. Methods

3.1. Sample preparation for microspectroscopic analysis

We analysed the volatile contents of experimental glasses using Fourier Transform Infrared spectroscopy (FTIR) and of fluid inclusions using confocal Raman microspectroscopy. In preparation for FTIR and Raman analysis, we gently cleaned the polished epoxy mounts containing the experimental run products with high purity ethanol and a small amount of 1 μm diamond paste to remove previous coatings of either carbon or gold. Volatile analysis of glass by FTIR requires the samples to be prepared as thin wafers so that light can pass through. We therefore removed the glassy experimental products from their platinum capsules and glued them to glass slides using thermoplastic resin. We then polished the samples using various particle size-grades of Al_2O_3 grinding paper to create glass wafers. Glass wafer thickness ranged from 117 to 145 μm and was measured using a digital micrometer with an accuracy of ±2 μm. We thinned the samples from the back of the epoxy mounts to preserve as much as possible the surface that was previously documented by SEM in Deegan et al. (2010). This approach allowed us to link the new volatile data to the textures and major element compositions of the glasses. Due to the abundance of vesicles and fractures permeating the experimental glasses, extracting the samples from the capsules was challenging, but several were successfully made into wafers with their original textural relationships intact. In total, glass from two hydrous experiments (runtimes = 0 and 300 s) plus a shard of the Merapi starting material glass were analysed by Fourier Transform Infrared spectroscopy (FTIR), while fluid inclusions (*i.e.* fluid-bearing bubbles or vesicles) in four hydrous experiments (runtimes = 0, 90, 150, and 300 s) were analysed using confocal Raman microspectroscopy.

3.2. Fourier transform infrared spectroscopy (FTIR) analysis of glass

FTIR spectra in the range 800–5000 cm^{-1} were acquired on glass wafers at the Swedish Museum of Natural History, Stockholm, Sweden, following a similar approach to that employed by Weis et al. (2015, 2016). The glasses were analysed using a Bruker Hyperion 2000 microscope equipped with a Globar source, a KBr beamsplitter, and an MCT (mercury-cadmium-telluride) detector. Cracks, vesicles and microcrystals in the glass were avoided by applying small apertures (100 to 200 μm) for masking during analysis. Analysis spots were selected with the aid of optical microscopy and SEM images of the glass wafers at various magnifications. A reference spectrum was acquired on epoxy resin to test for interferences from any traces of resin that may have intersected the beam path. The acquired spectra were baseline corrected using a polynomial function and the individual bands were fitted with the software *PeakFit*. For calculating volatile concentrations, we adopted a sample density of 2.5 g/cm^3. H_2O contents were calculated using the band at around 4500 cm^{-1} and an absorption coefficient of 0.67 $L \cdot mol^{-1} \cdot cm^{-1}$ (see Dixon et al., 1995; Shishkina et al., 2010). Molecular CO_2 contents were calculated using the band at around 2348 cm^{-1} and an absorption coefficient of 830 $L \cdot mol^{-1} \cdot cm^{-1}$ (see Behrens et al., 2004). CO_3 contents were calculated using the band at around 1430 cm^{-1} and an absorption coefficient of 317 $L \cdot mol^{-1} \cdot cm^{-1}$ (see Shishkina et al., 2010). Uncertainties on our volatile concentration results are based on uncertainties in sample thickness, density, and absorbance and are estimated at ±10%. Notably, we analysed a doubly polished wafer of the Merapi starting material glass for its H_2O content and replicated the previously obtained value for the same material, within error, as measured by Karl Fisher titration (see Deegan et al., 2010).

3.3. Confocal Raman microspectroscopy analysis of fluid inclusions

Confocal Raman microspectroscopy was conducted at the Research and Industrial Relations Center of the Faculty of Science, Eötvös Loránd University of Budapest, Hungary, using a HORIBA Jobin Yvon LabRAM HR 800 Raman microspectrometer. The method employed is similar to that described in Deegan et al. (2022). Raman analysis was carried out on μm-sized fluid inclusions beneath the surface of the glass wafers that were prepared for FTIR analysis. By focusing and defocusing the sample surface in reflected light, the internal reflections of spherical surfaces allowed us to locate and screen unexposed fluid inclusions in the glass wafers. Analysis spots were generally acquired from 2 to 42 μm below the surface of the wafers.

An OLYMPUS 100 × (N.A. = 0.9) objective was used to focus the laser on the analysed sites. We employed a frequency doubled Nd–YAG green laser with 532 nm excitation wavelength, displaying a power of 120 mW at the source and 23 mW on the sample surface for 100% laser power. We used a laser power spanning from 0.1 to 100% for experiment #379–17 and a constant laser power of 100% for all the other experiments. The Raman microspectrometer was calibrated before the measurements to the Rayleigh line at 0 cm^{-1}. Raman spectra acquisition was conducted at ambient temperature, in both single- and multi-window settings (from 1 to 11 windows) in a spectral range from 70 to 4200 cm^{-1}, with a spectral resolution of *ca.* 0.8 cm^{-1} above 3000 cm^{-1}. A 100 μm confocal hole, a 1800 grooves/mm optical grating, 2 accumulations, and a 30 s (in a few cases 60 and 90, and exceptionally up to 200 s) exposure time were employed for Raman analysis. The acquired spectra were baseline corrected and processed using the *LabSpec 5* software. The relative amounts of volatile species in the unexposed fluid inclusions were calculated using the integrated band areas of the acquired Raman spectra, after baseline correction, peak fitting, deconvolution, and conversion into a model ($n = 89$ out of 163 acquired Raman spectra).

In confocal Raman microspectroscopy, the detection limit exclusively depends on the Raman signal, thus universal detection limits are not available as measurements and samples cannot be standardized. However, the uncertainty on the calculated relative amounts of volatile species is estimated at ≤0.2 mol% (Berkesi et al., 2017). Minor residues from previous carbon coatings on the sample surfaces were also analysed using confocal Raman microspectroscopy in order to test for a potential contamination source. The very weak signal of the first order (main) Raman bands from the analysed residues of carbon coatings demonstrates that their contribution to the acquired Raman spectra is negligible. Similarly, the very weak signal of the Raman band from atmospheric N_2 (acquired at different depths in the host glass) demonstrates that its contribution to the acquired Raman spectra is also negligible.

3.4. Thermodynamic modelling and apparent diffusivity of CO_2

To explore the solubility behaviour of CO_2 in mafic melts that assimilated limestone, we used *SOLWCAD*, a Fortran code that computes the saturation surface of H_2O-CO_2 fluids in silicate melts (Papale et al., 2006). In this study, we calculated the CO_2-melt equilibrium (*i.e.* equilibrium dissolved CO_2) in the Ca-normal and Ca-rich experimental melts following the equations provided in Colucci et al. (2024). This approach accounts for the fact that assimilation of limestone changes the composition of the melts, which in turn contributes to changes in the volatile saturation surface (Papale et al., 2006). The *SOLWCAD* calculations require input of the melt composition and volatile content for the Ca-normal and Ca-rich melts, which requires knowledge of the amount of dissolved limestone in the melt. In this study we focussed on the 0 s and 300 s runtime experiments, since we obtained corresponding FTIR data for the glasses in those experiments. For the 0 s runtime experiment, we calculated equilibrium dissolved CO_2 in the Ca-normal and Ca-rich melts for two scenarios involving either 10 or 50% limestone assimilation. This is because the limestone xenolith is still visible in the 0 s runtime experimental end-product (Fig. 1f), so we assume that at least 10% but no more than 50% of the limestone xenolith was assimilated. For the 300 s runtime experiment, we carried out similar calculations, but since there is no limestone visible in the experimental end-product (Fig. 1h), we assumed complete assimilation.

When attempting to quantify the mobility of CO_2 in the magma–limestone experiments of this study, we emphasize that the experiments are kinetic and reflect the dynamic conditions present at the earliest phase of limestone assimilation in mafic melts. For instance, rapid bubble growth that took place within a few seconds of the experimental run time (Fig. 1c-h) likely induced perturbation of the melt and advective mass transfer. The magma–limestone experiments therefore differ from canonical diffusion couple experiments used to determine diffusivities due to chemical diffusion alone (*e.g.* Baker et al., 2005). For this reason, we refer to the diffusivity of CO_2 determined in this study as apparent diffusivity. Here, we calculated the apparent diffusivity of CO_2 (D_{CO2}) as the ratio between the thickness of the reacting melt layer (L) and the diffusion timescale (τ), where $D_{CO2} = L^2/\tau$. We employed the 0 s runtime experiment for our calculations, L = 0.5 mm (see Fig. 1f and Fig. 5a of Deegan et al., 2010), and τ = 100 s to account for the fact that limestone assimilation began during the isobaric heat-up stage (*i.e.* shortly before the experimental temperature was reached). The value for τ is the same as that used by Colucci et al. (2024) for calculating the apparent diffusivity of CaO in the same experiments.

4. Results

4.1. Results from FTIR and Raman analyses

The FTIR and Raman data obtained in this study are reported in full in the **Supplementary material** and summarised here. Representative spectra obtained from both methods are shown in Fig. 2. Analysis of the Merapi starting material glass by FTIR yielded H_2O = 2.0 wt% and CO_2 = 597 μg/g. The starting glass did not contain any molecular CO_2;

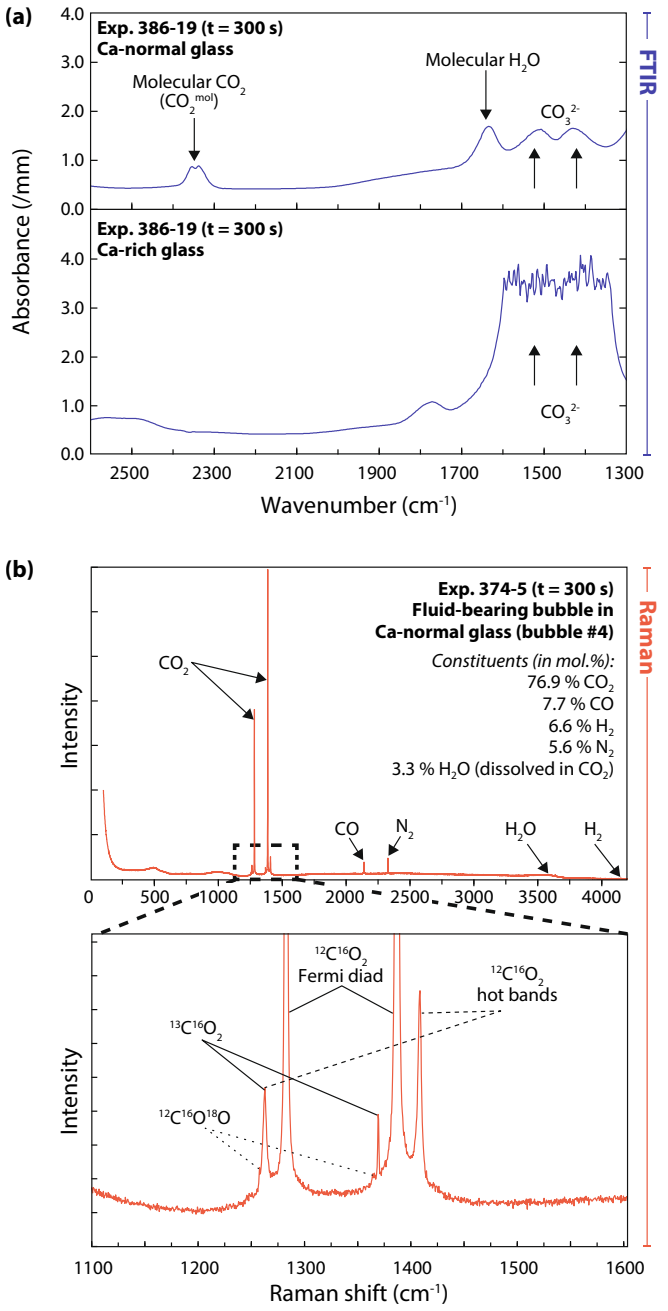

Fig. 2. **(a)** Midinfrared (FTIR) spectra of Ca-normal and Ca-rich glasses from experiment (Exp.) 386–19 (runtime = 300 s). Note that the CO_3^{2-} peaks in the Ca-rich glass are off-scale due to excessive absorption. **(b)** Raman spectrum acquired on a fluid inclusion in Ca-normal glass from experiment 374–5 (t = 300 s). A close-up of the CO_2 window shows the "Fermi diad" (sharp bands at 1285 cm^{-1} and 1388 cm^{-1}), the symmetrical "hot bands" (minor bands below 1285 cm^{-1} and above 1388 cm^{-1}, respectively), and the same Raman bands for CO_2 molecules containing ^{13}C and ^{18}O (*i.e.* CO_2 isotopologues).

instead all the CO_2 was found to be dissolved as the carbonate anion CO_3^{2-}, as commonly observed for basaltic and basaltic-andesitic glasses (Konschak and Keppler, 2014). Previous analysis of the same glass by Karl Fischer titration gave a water content of 2.2 wt% (Deegan et al., 2010), which compares well with our new results. Profiles showing FTIR CO_2 and H_2O contents through the glass in the 0 s runtime and 300 s runtime experiments are shown in Fig. 3 and Raman fluid inclusion results for 0, 90, 150, and 300 s runtime experiments are shown in Fig. 4.

In the shortest runtime magma–limestone interaction experiment (runtime = 0 s; Fig. 1f, Fig. 3a), the limestone is visible as it did not have enough time to fully dissolve into the host melt. The limestone is surrounded by a CaO-rich reacting melt (*Ca-rich glass*) that grades into the host melt (*Ca-normal glass*). Unlike the starting material glass, all glass in this experiment contains dissolved molecular CO_2 (written hereafter as CO_2^{mol}) with a mean of 664 μg/g (n = 12, where n is the number of FTIR data points) for the Ca-normal glass and 808 μg/g (n = 2) for the Ca-rich glass (Fig. 3b). The glass in this experiment is also strongly enriched in CO_3^{2-} with a mean of 2080 μg/g (n = 12) for the Ca-normal glass and 2239 μg/g (n = 2) for the Ca-rich glass (Fig. 3c). Total CO_2 (written hereafter as CO_2^{tot}) is the sum of CO_2^{mol} and CO_3^{2-} and is shown in Fig. 3d. Regarding water contents of the glasses, the Ca-normal and Ca-rich glasses do not differ significantly and have an overall mean H_2O content of 2.1 wt% (n = 14; Fig. 3e), which is indistinguishable from the starting material glass.

In the longest runtime magma–limestone interaction experiment (runtime = 300 s; Fig. 1h, Fig. 3f), the limestone fragment is no longer visible as it completely dissolved into the melt, yielding a volumetrically large Ca-rich glass domain and relatively large bubbles. Similar to the 0 s runtime experiment, the Ca-normal glass in the 300 s runtime experiment contains CO_2^{mol}, with a mean of 516 μg/g (n = 13). However, CO_2^{mol} was notably absent from the Ca-rich glass in this experiment (Figs. 2a, 3g). The Ca-normal glass contains on average 1918 μg/g (n = 13) of CO_3^{2-}, but the Ca-rich glass contains such a high concentration of CO_3^{2-} that its content could not be quantified because the CO_3^{2-} peaks were off-scale due to excessive absorption (Fig. 2a, Fig. 3h-i). The Ca-normal and Ca-rich glasses also differ in terms of their average H_2O contents of 2.0 wt% H_2O (n = 13) and 1.2 wt% (n = 8), respectively (Fig. 3j).

In fluid inclusions, the most abundant volatile species is CO_2, accompanied by minor, but variable, amounts of CO, CH_4, N_2, H_2, and H_2O (Fig. 2b, Fig. 4). Also detected were H_2S and C_2H_6, but only rarely and at very low abundances (≤ 0.1 mol%). Fluid inclusions in Ca-normal glass contain the greatest species diversity and possess on average 16 to 33 mol% of $CH_4 + N_2 + CO + H_2 + H_2O$ and 67 to 84 mol% CO_2, based on the measurement of multiple fluid inclusions in four experiments of differing runtimes (Fig. 4b-c). In Ca-rich glass, fluid inclusions in the experiment with runtime = 0 s contain on average 20 mol% of $CO + N_2$ and 80 mol% CO_2. However, in experiments with longer runtimes, fluid inclusions in Ca-rich glass contain on average 3 to 4 mol% of $CO + H_2O + H_2 + N_2$ and ≥ 96 mol% CO_2 (Fig. 4b, d-e).

Since confocal Raman microspectroscopy cannot discern between liquid H_2O trapped in fluid inclusions and molecular H_2O contained in the host glass, only H_2O dissolved in CO_2 can be quantified as being exclusively derived from the fluid inclusions. The comparison between Raman spectra of the fluid inclusions, their rim, and their host glass indicate that additional H_2O may occur as liquid H_2O in thin films along fluid inclusion boundaries in at least some cases. However, the undetectability of these thin films of liquid H_2O in the fluid inclusions by optical microscopy suggests a H_2O content of ≤20 mol% (Frezzotti et al., 2012). Since the H_2O content of fluid inclusions in this study was exclusively quantified as H_2O dissolved in CO_2, it thus corresponds to a minimum estimate. We also note that a characteristic Raman band of carbonates (at *ca.* 720 cm^{-1} Raman shift) was detected during analysis of fluid inclusions in Ca-rich glass. The presence of a carbonate Raman band likely reflects the extremely high concentration of dissolved CO_3^{2-} in the Ca-rich glass, as corroborated by the FTIR data and thermodynamic modelling (see below).

4.2. *Results from thermodynamic modelling and diffusivity calculations*

The equilibrium dissolved CO_2 values produced by *SOLWCAD* are for total CO_2 (CO_2^{tot}), which is the sum of CO_2^{mol} and CO_3^{2-}. This is important to bear in mind when comparing to the FTIR results, since FTIR allows us to distinguish between CO_2^{mol} and CO_3^{2-}. Using *SOLWCAD*, we found that the equilibrium dissolved CO_2 in the Ca-normal melt in the 0 s runtime experiment is 3654 μg/g and 3663 μg/g for 10% and 50% limestone assimilation, respectively. In the 300 s runtime experiment, the

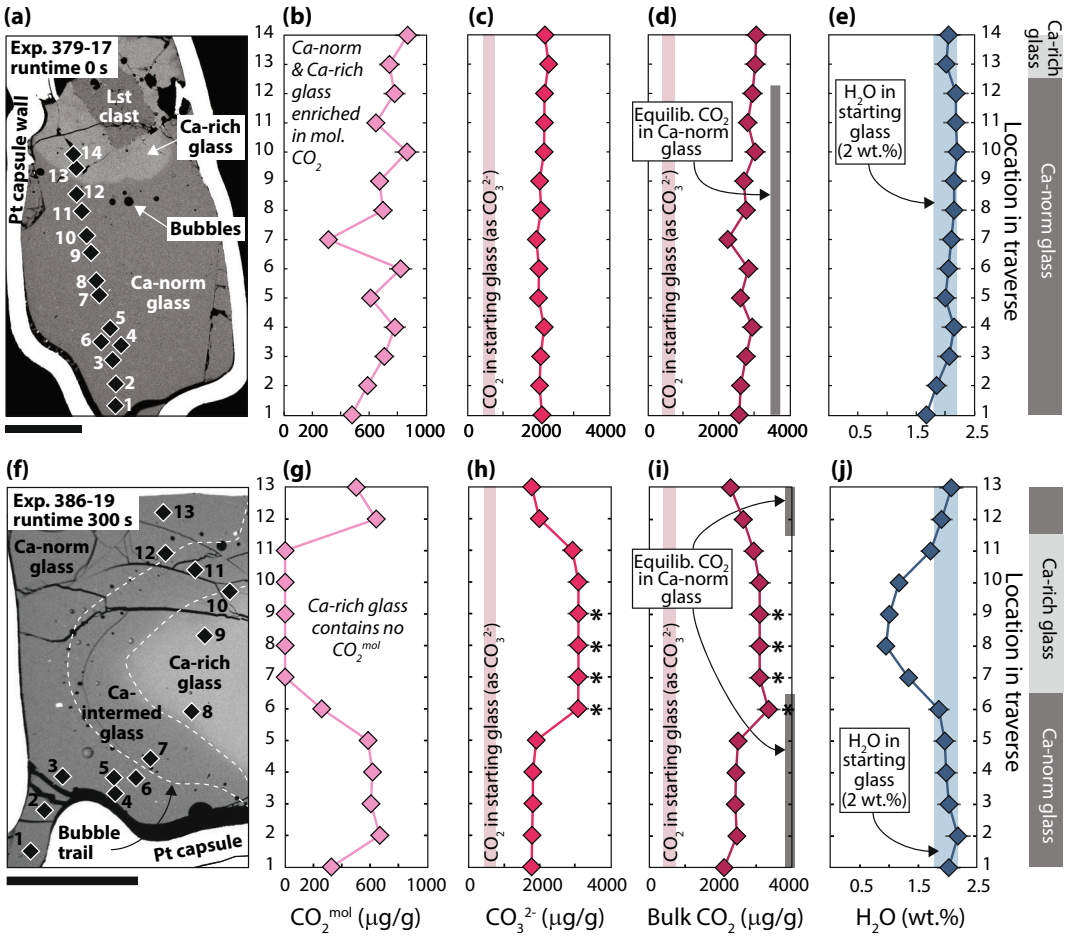

Fig. 3. **(a)** SEM image of experiment (Exp.) with runtime = 0 s showing locations of FTIR analysis spots. **(b-e)** CO_2^{mol}, CO_3^{2-}, bulk (total) CO_2, and H_2O glass profiles. **(f)** SEM image of experiment with runtime = 300 s showing locations of FTIR analysis spots. **(g-j)** CO_2^{mol}, CO_3^{2-}, bulk (total) CO_2, and H_2O glass profiles. Asterisks in **(h)** and **(i)** indicate that the values are minima because the CO_3^{2-} vibrations in the Ca-rich glass were too strong to be resolved. Grey bars in panels **(d)** and **(i)** show *SOLWCAD* equilibrium dissolved CO_2 contents in the Ca-normal glass, which are similar to the estimated overall solubility of CO_2 in the starting material glass. *SOLWCAD* equilibrium dissolved CO_2 contents for the Ca-rich glass plot off-scale and range from 9300 to 40,944 µg/g CO_2, depending on the amount of assimilated limestone. Note that in the 300 s experiment, all CO_2 in the Ca-rich glass is dissolved as the carbonate anion while the co-existing fluid is comprised of CO_2 molecules. See text for further details. Abbreviations: Ca-intermed = Ca-intermediate; Equilib = equilibrium.

equilibrium dissolved CO_2 in the Ca-normal melt is 4027 µg/g. Equilibrium dissolved CO_2 in the Ca-rich melts in the 0 s runtime experiment ranges from 9300 to 40,944 µg/g for 10% and 50% limestone assimilation, respectively, whereas in the 300 s runtime experiment it is 38,710 µg/g. Regarding diffusivity of CO_2, our calculation gave an apparent diffusivity (D_{CO2}) $\gtrsim 10^{-7}$ m^2/s.

5. Discussion

5.1. CO_2 solubility in the experimental melts

For mafic melts similar in composition to the Merapi starting material, at the P-T conditions employed for the experiments in this study, the solubility of CO_2 is around 3000 to 4000 µg/g (Papale et al., 2006). This range encompasses the equilibrium dissolved CO_2 for Ca-normal melt in the experiments calculated by *SOLWCAD*. Therefore, the Merapi starting glass is undersaturated in CO_2, since its CO_2^{tot} is relatively low, at 597 µg/g. Once assimilation began, however, CO_2 fluxed through the host melt, as observed in the 0 s runtime experiment, where the Ca-normal and Ca-rich glass contain mean CO_2^{tot} of 2744 and 3047 µg/g, respectively. We observe that the Ca-normal and Ca-rich glasses in the 0 s runtime experiment contain CO_2^{mol} and CO_3^{2-} molecules. The presence of both forms of CO_2 in both types of glass in the 0 s runtime experiments demonstrates unequivocally that CO_2 was liberated from limestone during the experiment heat-up phase, before the target temperature at 0 s was reached (Fig. 3b-d).

The 300 s runtime experiment represents the case where limestone assimilation reached completion. In this experiment, we find that the Ca-normal glass contains mean CO_2^{tot} of 2434 µg/g, which is similar to the mean CO_2^{tot} content of the Ca-normal glass in the 0 s runtime experiment. In contrast, the Ca-rich glass in the 300 s runtime experiment is extremely enriched in CO_2 (dissolved as CO_3^{2-}), so much so that its quantity could not be resolved from the FTIR spectra (Fig. 2a). Based on our *SOLWCAD* calculations, CO_2 in the Ca-rich glass could be more than 10 times greater than in the Ca-normal glass (up to *ca.* 40,000 µg/g). The high CO_2 concentration in the Ca-rich glass may be explained by the positive influence of melt CaO content on overall CO_2 solubility (Papale et al., 2006; Iacono-Marziano et al., 2012). However, it is important to note that the Ca-rich glass in the 300 s runtime experiment is devoid of molecular CO_2 (Fig. 3g and h). The absence of CO_2^{mol} in this glass can be explained by partitioning of CO_2 molecules into the increasingly voluminous fluid phase, as corroborated by our Raman fluid inclusion data (Fig. 4d). The Ca-rich glass in the 300 s runtime experiment is also relatively depleted in H_2O (Fig. 3j), pointing to exsolution of water from the Ca-contaminated melt. Water degassing from the melt is again supported by the Raman data, which show increasing H_2O contents of fluid inclusions in the Ca-rich glass over time (Fig. 4e).

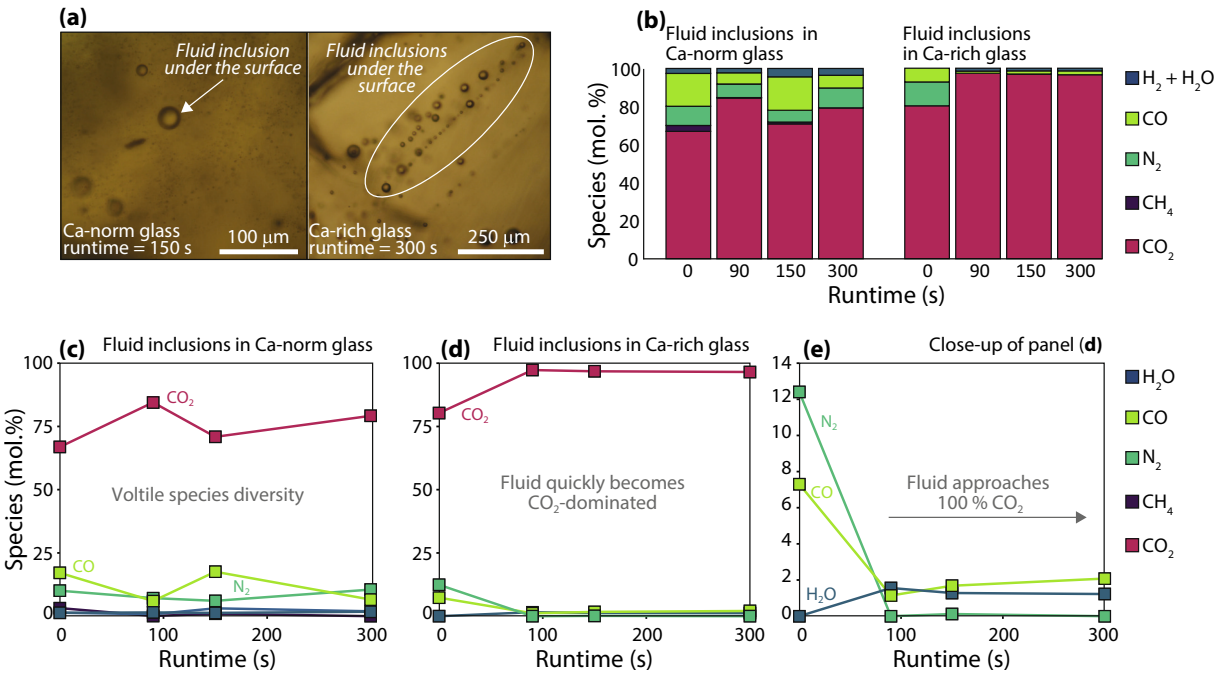

Fig. 4. **(a)** Transmitted light photomicrographs of two experiments showing unexposed fluid inclusions. **(b)** Stacked bar charts of volatile species abundance in fluid inclusions analysed in Ca-normal and Ca-rich glass, respectively (average values per glass type per experiment; see Supplementary material). **(c-e)** Variations in volatile species abundance in fluid inclusions analysed in Ca-normal glass and Ca-rich glass with increasing experiment runtime (average values per glass type per experiment; see Supplementary material). The H_2O content of fluid inclusions is exclusively quantified as H_2O dissolved in CO_2 and does not consider liquid H_2O along fluid inclusion boundaries. The H_2O contents shown are therefore minimum estimates.

5.2. *Apparent diffusivity of CO_2 during limestone assimilation*

The experiments show that from the onset of limestone assimilation, CO_3^{2-} and CO_2^{mol} move away from the limestone xenolith and migrate through the Ca-rich reacting melt and the surrounding Ca-normal host melt (Fig. 3). We can therefore deduce that CO_3^{2-} and CO_2^{mol} have greater mobilities than CaO during limestone assimilation. Because chemical diffusion is a key mechanism of limestone assimilation and volatile transport in the host melt (Colucci et al., 2024), we quantified the apparent diffusivity of CO_2 in the experiments and found that $D_{CO2} \gtrsim 10^{-7}$ m^2/s. The apparent diffusivity of CO_2 calculated here is extremely fast compared to silicate melts such as basalt or trachyte, where D_{CO2} is typically on the order 10^{-12} to 10^{-11} (see Baker et al., 2005 and **Supplementary material**). Furthermore, D_{CO2} in our experiments is at least one order of magnitude higher than the corresponding D_{CaO}, which ranges from 10^{-11} to 10^{-7} m^2/s (Colucci et al., 2024). The higher apparent diffusivity of CO_2 compared to CaO at the onset of limestone assimilation explains how all glass in the 0 s runtime experiment is enriched in CO_2, while Ca-enrichment of the glass in the same experiment is restricted to the limestone-melt interface layer (*i.e.* the reacting melt).

We are not aware of diffusivity studies on short-term magma–limestone interaction experiments in the literature, but we point out that a small number of reconnaissance calcite assimilation experiments were performed by Baker et al. (2005) in the context of a wider volatile diffusion study. In Baker et al. (2005), the authors allowed calcite to dissolve into trachytic melts at $P = 1$ GPa and $T = 1100$ or 1200 °C. They then estimated the CO_2 contents of the resulting glasses using the "difference from 100 %" electron microprobe technique (see Devine et al., 1995) and calculated D_{CO2} values on the order of 10^{-13} to 10^{-12} m^2/s. These values are much lower than the D_{CO2} values calculated here, but since Baker et al. (2005) do not provide information on experiment runtimes or whether bubbles were present or not in the run products, it is unlikely that their experiments are directly comparable to ours. The extremely fast apparent CO_2 diffusivity recorded here is likely the result of the specific design of the magma–limestone interaction experiments analysed here, whereby the dynamic processes of assimilation and degassing present at the onset of limestone assimilation were captured in the experimental run products. In this context, we posit that fluid overpressure from CO_2 bubble nucleation and growth at the limestone-melt interface induced localised strain, which in turn decreased melt viscosity and promoted enhanced diffusivity. This mechanism was also proposed by Colucci et al. (2024) to explain the anomalously high apparent diffusivity of CaO and the distinctive shape of the concentration profile of CaO observed in the same experiments. Therefore, an actively developing fluid pressure gradient during limestone assimilation causes CO_2 to flux through the local melt environment. We also suggest that fluid overpressure at the limestone-melt interface is time-dependent. In other words, if the assimilation experiments had been conducted with longer runtimes, the system would have become more homogenised and the evidence for rapid CO_2 fluxing would have been lost.

5.3. *Carbon assimilation by mafic melts*

In the previous sections, we established that CO_3^{2-} and CO_2^{mol} moved rapidly through both the Ca-rich reacting melt and the Ca-normal host melt. However, despite being contaminated with limestone-derived CO_2, the Ca-normal host melt displays no sign of limestone assimilation in terms of its major element composition. This can be explained by the higher apparent diffusivity of CO_2 compared to CaO during limestone assimilation, which causes decoupling of CO_2 and CaO based on their differing mobilities. Limestone assimilation can therefore cause mafic melts to receive a flush of limestone-derived CO_2, while imparting little to no change to major element compositions. Carbon contamination of mafic melts due to limestone assimilation may thus be considered cryptic, since it is difficult to identify using standard whole-rock geochemistry.

This realization is crucial because the role of limestone assimilation is sometimes assumed to be minimal based on whole-rock arc lava

compositions that lack significant Ca enrichment. A case in point is Merapi volcano, Indonesia, where the major element geochemistry of erupted lavas do not display strong evidence for limestone assimilation (*e.g.,* Costa et al., 2013; Handley et al., 2014). Yet, studies spanning multiple isotope systems, including of the volatile elements oxygen and carbon, have convincingly demonstrated the effects of magma–limestone interaction on gas, mineral, and whole-rock isotopic compositions at Merapi (*e.g.,* Chadwick et al., 2007; Troll et al., 2012, 2013; Borisova et al., 2013; Whitley et al., 2019; Deegan et al., 2021).

As shown in this study, magma–limestone interaction causes CO_2 to flux rapidly through the host melt, transferring ^{13}C and ^{18}O (limestone-derived isotopes of C and O) to the magma system. Volcanic CO_2 with high $^{13}C/^{12}C$ ratios (*i.e.* high $\delta^{13}C$ values) has been detected in volcanic arc emissions and used as an indicator of remobilized crustal carbon in Indonesia and elsewhere (Troll et al., 2012; Mason et al., 2017). Moreover, since CO_2 is an oxygen-rich volatile, when it fluxes into the melt it can induce oxygen isotopic exchange. Experiments on the kinetics of oxygen isotope exchange between CO_2 vapour and silica glass have shown that isotopic exchange is controlled by diffusion of CO_2 molecules into the glass followed by exchange with oxygen in the glass structure (Stolper and Epstein, 1991). Moreover, it is the rate of diffusion of CO_2 molecules through the melt governs the rate of oxygen isotope exchange (Stolper and Epstein, 1991). Since CO_2 flushes rapidly through the host melt during magma–limestone interaction ($D_{CO2} \gtrsim 10^{-7}$ m^2/s), it is plausible that oxygen with a high $^{18}O/^{16}O$ ratio (*i.e.* high $\delta^{18}O$ value) would re-equilibrate with the melt over time periods of hours to days (Dallai et al., 2011). This process may therefore lead to detectable changes in the $\delta^{18}O$ value of crystallizing minerals without impacting the overall major element composition of the melt (see Dallai et al., 2011; Deegan et al., 2021).

Furthermore, although Ca is liberated during magma–limestone interaction, it can be taken up by the formation of skarn minerals, thus resulting in relatively small changes to overall melt compositions in terms of their CaO contents (*e.g.,* Spandler et al., 2012; Whitley et al., 2020). Skarn formation is likely to be more prominent in the shallower portions of magma plumbing systems, after the magma has evolved to higher silica compositions (Carter and Dasgupta, 2016). In contrast, CO_2 fluxing from limestone is potentially a very important process in the mid- to shallow-crustal portions of magma plumbing systems, when relatively hot, mafic magmas are emplaced into limestone and/or marble bedrock or when mafic melts are injected into pre-existing magma reservoirs as replenishing magmas. Intrusion of limestone by mafic magma is the scenario best represented by this study, wherein CO_2 fluxes through the host melt as a consequence of magma–limestone interaction. Remarkably, the results of this study now provide a process-based experimental underpinning for earlier models of magma reservoirs emplaced into limestone bedrock. For example, the work by Freda et al. (1997) proposed that CO_2-fluids migrated from limestone bedrock into the Villa Senni (Alban Hills, Italy) magma reservoir and exerted a fundamental control on magmatic evolution. Furthermore, extra CO_2 from limestone would increase the buoyancy of the magma and, if the CO_2-rich mafic magma ascended and intersected a shallower magma reservoir, it would force the exsolution of CO_2 and potentially promote explosive eruptive behaviour (*e.g.,* Freda et al., 2010).

We emphasize that it can be difficult to determine the significance of limestone assimilation based on bulk magma chemistry and, in turn, the fate of CO_2 liberated from assimilated limestone. Since silicate melts are the main carriers of carbon from the Earth's interior to surface (Ni and Keppler, 2013), magmas that are rich in limestone-derived CO_2 may play an underappreciated role in modulating carbon outgassing and hence the carbon inventory of arc volcanoes.

6. Summary and wider implications

The processes involved in assimilation of limestone xenoliths by mafic melts are summarised in Fig. 5. In brief, limestone assimilation

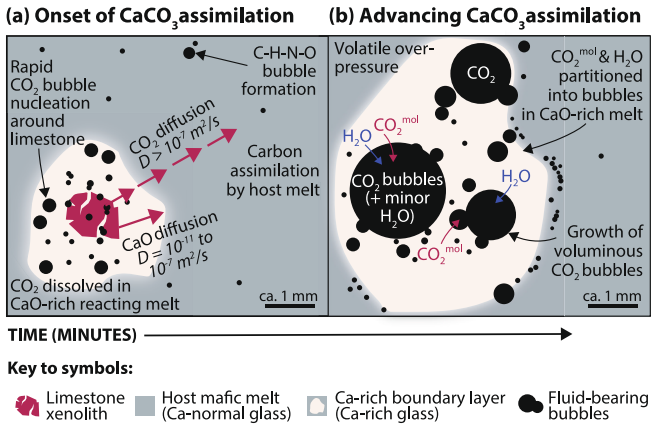

Fig. 5. Sketch summarising the processes involved in assimilation of millimetric sized limestone xenoliths in mafic magma over a timescale of several minutes. Panel **(a)** shows the earliest stage of limestone assimilation as represented by the 0 s runtime magma–limestone interaction experiment, while panel **(b)** shows the advanced stage limestone assimilation as represented the 300 s runtime experiment. This study shows that when mafic melt ascends through the crust and interacts with limestone, the melt can become enriched in CO_2 while showing no other obvious signs of contamination. Mafic melts in volcanic regions underlain by limestone may thus become silent carriers of carbon through magmatic plumbing systems.

causes formation of a CaO-rich silicate boundary layer (reacting melt) at the magma–limestone interface and generation of CO_2 bubbles, which establishes a fluid pressure gradient extending away from the limestone. The local melt near the magma–limestone interface becomes saturated in CO_2 over a timescale of minutes (for millimetric sized xenoliths) as CO_2 fluxes through the melt. Our experiments show that, during limestone assimilation, CO_2 moves through the melt at a rate of *ca.* one order of magnitude faster than CaO. The relatively high apparent diffusivity of CO_2 during magma–limestone interaction is likely maintained for so long as the fluid overpressure is high, *i.e.*, while bubbles are actively forming at the limestone–melt interface. Mixed volatile bubbles nucleate and grow in the host melt, whereas bubbles in the Ca-rich boundary layer surrounding the xenolith increase their CO_2 and H_2O contents by taking up CO_2 released by the actively degassing and dissolving limestone and by extraction of CO_2 and H_2O molecules from the melt. Bubbles in the Ca-rich melt quickly evolve to contain almost 100% CO_2 in the case of pure calcite assimilation, as is represented by our experiments. Crucially, since CO_2 migrates more quickly through the host melt than CaO, the host melt can become cryptically contaminated with limestone-derived carbon. This realization implies that mafic melts that interacted with calcite can be transformed into silent carriers of carbon through magmatic systems.

A key implication from our new volatile data is that fluxing of CO_2 from limestone assimilation can impact the carbon inventory, rheological properties, density, and explosive potential of magmas. These effects will be temporarily enhanced in situations where new xenolith reaction surface area becomes available due to earthquake-induced rock fracturing, dyking, or thermal shattering of xenoliths (*e.g.,* Troll et al., 2012; Carr et al., 2018; Deegan et al., 2022). Therefore, CO_2 fluxing at limestone-intersecting volcanoes may be a more important contributor to eruption dynamics, magmatic carbon fluxes, and long-term climate change than previously assumed. These conclusions apply to arc volcanoes built upon limestone crustal successions, but also to any volcanic environment where mafic magma potentially interacted with limestone, such as at Large Igneous Provinces (LIPs) emplaced in sedimentary basins.

CRediT authorship contribution statement

Frances M. Deegan: Writing – review & editing, Writing – original draft, Visualization, Validation, Resources, Project administration, Methodology, Investigation, Funding acquisition, Formal analysis, Data curation, Conceptualization. **Manfredo Capriolo:** Writing – review & editing, Visualization, Validation, Methodology, Investigation, Formal analysis, Data curation, Conceptualization. **Valentin R. Troll:** Writing – review & editing, Resources, Methodology, Funding acquisition, Conceptualization. **Franz A. Weis:** Writing – review & editing, Visualization, Methodology, Investigation, Formal analysis, Data curation. **Sara Callegaro:** Writing – review & editing, Funding acquisition, Conceptualization. **Simone Colucci:** Writing – review & editing, Software, Methodology, Investigation, Conceptualization. **Carmela Freda:** Writing – review & editing, Resources, Methodology, Conceptualization. **Valeria Misiti:** Writing – review & editing, Resources, Methodology. **László E. Aradi:** Writing – review & editing, Methodology. **Henrik Skogby:** Writing – review & editing, Methodology. **Herlan Darmawan:** Writing – review & editing. **Harri Geiger:** Writing – review & editing.

Declaration of competing interest

The authors declare the following financial interests/personal relationships which may be considered as potential competing interests: Frances M Deegan reports financial support was provided by Swedish Research Council. Valentin Troll reports financial support was provided by European Research Council. Sara Callegaro reports financial support was provided by Norwegian Research Council. Sara Callegaro reports financial support was provided by European Research Council. If there are other authors, they declare that they have no known competing financial interests or personal relationships that could have appeared to influence the work reported in this paper.

Acknowledgements

We are grateful to S. Mollo and an anonymous reviewer for thoughtful comments that improved the manuscript. We thank M. Nazzari for microprobe assistance at INGV Rome and C. Szabó for access to the Raman microspectroscopy laboratory at Eötvös Loránd University of Budapest. FMD thanks T. Pharasyn for invaluable support during the finalization of this work. The starting materials were sampled with permission from GEOTECHNOLOGIEN of BMBF and DFG (grant 03G0578A), linked to the SUNDAARC agreement between the Federal Institute for Geosciences and Natural Resources of the Federal Republic of Germany and the Directorate General of Geology and Mineral Resources of the Republic of Indonesia. This work was made possible with funding from the Swedish Research Council to FMD (grants 2018-04933 and 2022-04569). VRT acknowledges additional financial support from ERC project "ROTTnROCK", a research project funded by the European Research Council under the European Union's Horizon Europe Programme/ERC Synergy Grant (ERC-2023-SyG 101118491). SC acknowledges additional financial support from the Norwegian Research Council (Young Talent grant 301096) and the ERC project "DEGAS", a research project funded by the European Research Council under the European Union's Horizon Europe Programme/ERC Consolidator Grant (ERC-2024-CoG 101170872).

Appendix A. Supplementary data

Supplementary data to this article can be found online at https://doi.org/10.1016/j.chemgeo.2026.123264.

Data availability

The data underlying this work are reported in the manuscript and its supplementary materials.

References

Aiuppa, A., Fischer, T.P., Plank, T., Robidoux, P., Di Napoli, R., 2017. Along-arc, inter-arc and arc-to-arc variations in volcanic gas CO_2/S_T ratios reveal dual source of carbon in arc volcanism. Earth-Sci. Rev. 168, 24–47. https://doi.org/10.1016/j.earscirev.2017.03.005.

Baker, D.R., Freda, C., Brooker, R.A., Scarlato, P., 2005. Volatile diffusion in silicate melts and its effects on melt inclusions. Ann. Geophys. 48, 699–717.

Barnes, C.G., Prestvik, T., Sundvoll, B., Surratt, D., 2005. Pervasive assimilation of carbonate and silicate rocks in the Hortavaer igneous complex, north-central Norway. Lithos 80, 179–199. https://doi.org/10.1016/j.lithos.2003.11.002.

Behrens, H., Ohlhorst, S., Holtz, F., Champenois, M., 2004. CO_2 solubility in dacitic melts equilibrated with H_2O-CO_2 fluids: implications for modeling the solubility of CO_2 in silicic melts. Geochim. Cosmochim. Acta 68, 4687–4703. https://doi.org/10.1016/j.gca.2004.04.019.

Berkesi, M., Káldos, R., Park, M., Szabó, C., Váczi, T., Török, K., Németh, B., Czuppon, G., 2017. Detection of small amounts of N_2 in CO_2-rich high-density fluid inclusions from mantle xenoliths. Eur. J. Mineral. 29, 423–431. https://doi.org/10.1127/ejm/2017/0029-2615.

Blythe, L.S., Deegan, F.M., Freda, C., Jolis, E.M., Masotta, M., Misiti, V., Taddeucci, J., Troll, V.R., 2015. CO_2 bubble generation and migration during magma–carbonate interaction. Contrib. Mineral. Petrol. 169, 1–16. https://doi.org/10.1007/s00410-015-1137-4.

Borisova, A.Y., Martel, C., Gouy, S., Pratomo, I., Sumarti, S., Toutain, J.P., Bindeman, I. N., de Parseval, P., Metaxian, J.P., Surono, 2013. Highly explosive 2010 Merapi eruption: evidence for shallow-level crustal assimilation and hybrid fluid. J. Volcanol. Geotherm. Res. 261, 193–208. https://doi.org/10.1016/j.jvolgeores.2012.11.002.

Carr, B.B., Clarke, A.B., de Michieli Vitturi, M., 2018. Earthquake induced variations in extrusion rate: a numerical modeling approach to the 2006 eruption of Merapi Volcano (Indonesia). Earth Planet. Sci. Lett. 482, 377–387. https://doi.org/10.1016/j.epsl.2017.11.019.

Carter, L.B., Dasgupta, R., 2015. Hydrous basalt-limestone interaction at crustal conditions: implications for generation of ultracalcic melts and outflux of CO_2 at volcanic arcs. Earth Planet. Sci. Lett. 427, 202–214. https://doi.org/10.1016/j.epsl.2015.06.053.

Carter, L.B., Dasgupta, R., 2016. Effect of melt composition on crustal carbonate assimilation: implications for the transition from calcite consumption to skarnification and associated CO_2 degassing. Geochem. Geophys. Geosyst. 17, 3893–3916. https://doi.org/10.1002/2015GC006171.Received.

Carter, L.B., Dasgupta, R., 2018. Decarbonation in the Ca-Mg-Fe carbonate system at mid-crustal pressure as a function of temperature and assimilation with arc magmas – implications for long-term climate. Chem. Geol. 492, 30–48. https://doi.org/10.1016/j.chemgeo.2018.05.024.

Chadwick, J.P., Troll, V.R., Ginibre, C., Morgan, D., Gertisser, R., Waight, T.E., Davidson, J.P., 2007. Carbonate assimilation at Merapi volcano, Java, Indonesia: insights from crystal isotope stratigraphy. J. Petrol. 48, 1793–1812. https://doi.org/10.1093/petrology/egm038.

Colucci, S., Brogi, F., Sottili, G., Montagna, C.P., Papale, P., 2024. Short-term magma-carbonate interaction: a modelling perspective. Earth Planet. Sci. Lett. 628, 118592. https://doi.org/10.1016/j.epsl.2024.118592.

Costa, F., Andreastuti, S., Bouvet de Maisonneuve, C., Pallister, J.S., 2013. Petrological insights into the storage conditions, and magmatic processes that yielded the centennial 2010 Merapi explosive eruption. J. Volcanol. Geotherm. Res. 261, 209–235. https://doi.org/10.1016/j.jvolgeores.2012.12.025.

Dallai, L., Cioni, R., Boschi, C., D'Oriano, C., 2011. Carbonate-derived CO_2 purging magma at depth: influence on the eruptive activity of Somma-Vesuvius, Italy. Earth Planet. Sci. Lett. 310, 84–95. https://doi.org/10.1016/j.epsl.2011.07.013.

Deegan, F.M., Troll, V.R., Freda, C., Misiti, V., Chadwick, J.P., McLeod, C.L., Davidson, J. P., 2010. Magma-carbonate interaction processes and associated CO_2 release at Merapi volcano, Indonesia: insights from experimental petrology. J. Petrol. 51, 1027–1051. https://doi.org/10.1093/petrology/egq010.

Deegan, F.M., Troll, V.R., Whitehouse, M.J., Jolis, E.M., Freda, C., 2016. Boron isotope fractionation in magma via crustal carbonate dissolution. Sci. Rep. 6, 1–7. https://doi.org/10.1038/srep30774.

Deegan, F.M., Whitehouse, M.J., Troll, V.R., Geiger, H., Jeon, H., le Roux, P., Harris, C., van Helden, M., González-Maurel, O., 2021. Sunda arc mantle source $\delta^{18}O$ value revealed by intracrystal isotope analysis. Nat. Commun. 12, 3930. https://doi.org/10.1038/s41467-021-24143-3.

Deegan, F.M., Bédard, J.H., Grasby, S.E., Dewing, K., Geiger, H., Misiti, V., Capriolo, M., Callegaro, S., Svensen, H.H., Yakymchuk, C., Aradi, L.E., Freda, C., Troll, V.R., 2022. Magma–shale interaction in large igneous provinces: implications for climate warming and sulfide genesis. J. Petrol. 63, 1–10. https://doi.org/10.1093/petrology/egac094.

Deegan, F.M., Troll, V.R., Gertisser, R., Freda, C., 2023. Magma-carbonate interaction at Merapi volcano, Indonesia. In: Gertisser, R., et al. (Eds.), Merapi Volcano, Active Volcanoes of the World. Springer, pp. 291–321. https://doi.org/10.1007/978-3-031-15040-1_10.

Devine, J.D., Gardner, J.E., Brack, H.P., Layne, G.D., Rutherford, M.J., 1995. Comparison of microanalytical methods for estimating H_2O contents of silicic volcanic glasses. Am. Mineral. 80, 319–328. https://doi.org/10.2138/am-1995-3-413.

Di Rocco, T., Freda, C., Gaeta, M., Mollo, S., Dallai, L., 2012. Magma chambers emplaced in carbonate substrate: Petrogenesis of skarn and cumulate rocks and implications for CO_2 degassing in volcanic areas. J. Petrol. 53, 2307–2332. https://doi.org/10.1093/petrology/egs051.

Dixon, J.E., Stolper, E.M., Holloway, J.R., 1995. An experimental study of water and carbon dioxide solubilities in Mid-Ocean Ridge basaltic liquids. Part I: calibration and solubility models. J. Petrol. 36, 1607–1631. https://doi.org/10.1093/oxfordjournals.petrology.a037267.

Erdmann, S., Martel, C., Pichavant, M., Bourdier, J.L., Champallier, R., Komorowski, J. C., Cholik, N., 2016. Constraints from phase equilibrium experiments on pre-eruptive storage conditions in mixed magma systems: a case study on crystal-rich basaltic andesites from Mount Merapi, Indonesia. J. Petrol. 57, 535–560. https://doi.org/10.1093/petrology/egw019.

Freda, C., Gaeta, M., Palladino, D.M., Triglia, R., 1997. The Villa Senni Eruption (Alban Hills, Central Italy): the role of H_2O and CO_2 on the magma chamber evolution and on the erutive scenario. J. Volcanol. Geotherm. Res. 78, 103–120. https://doi.org/10.1016/S0377-0273(97)00007-3.

Freda, C., Gaeta, M., Misiti, V., Mollo, S., Dolfi, D., Scarlato, P., 2008. Magma-carbonate interaction: an experimental study on ultrapotassic rocks from Alban Hills (Central Italy). Lithos 101, 397–415. https://doi.org/10.1016/j.lithos.2007.08.008.

Freda, C., Gaeta, M., Giaccio, B., Marra, F., Palladino, D.M., Scarlato, P., Sottili, G., 2010. CO_2-driven large mafic explosive eruptions: the Pozzolane Rosse case study from the Colli Albani Volcanic District (Italy). Bull. Volcanol. 73, 241–256. https://doi.org/10.1007/s00445-010-0406-3.

Frezzotti, M.L., Tecce, F., Casagli, A., 2012. Raman spectroscopy for fluid inclusion analysis. J. Geochem. Explor. 112, 1–20. https://doi.org/10.1016/j.gexplo.2011.09.009.

Gaeta, M., Di Rocco, T., Freda, C., 2009. Carbonate assimilation in open magmatic systems: the role of melt-bearing skarns and cumulate-forming processes. J. Petrol. 50, 361–385. https://doi.org/10.1093/petrology/egp002.

Gozzi, F., Gaeta, M., Freda, C., Mollo, S., Di Rocco, T., Marra, F., Dallai, L., Pack, A., 2014. Primary magmatic calcite reveals origin from crustal carbonate. Lithos 190–191, 191–203. https://doi.org/10.1016/j.lithos.2013.12.008.

Handley, H.K., Blichert-Toft, J., Gertisser, R., Macpherson, C.G., Turner, S.P., Zaennudin, A., Abdurrachman, M., 2014. Insights from Pb and O isotopes into along-arc variations in subduction inputs and crustal assimilation for volcanic rocks in Java, Sunda arc, Indonesia. Geochim. Cosmochim. Acta 139, 205–226. https://doi.org/10.1016/j.gca.2014.04.025.

Iacono Marziano, G., Gaillard, F., Pichavant, M., 2007. Limestone assimilation and the origin of CO_2 emissions at the Alban Hills (Central Italy): constraints from experimental petrology. J. Volcanol. Geotherm. Res. 166, 91–105. https://doi.org/10.1016/j.jvolgeores.2007.07.001.

Iacono Marziano, G., Gaillard, F., Pichavant, M., 2008. Limestone assimilation by basaltic magmas: an experimental re-assessment and application to Italian volcanoes. Contrib. Mineral. Petrol. 155, 719–738. https://doi.org/10.1007/s00410-007-0267-8.

Iacono-Marziano, G., Gaillard, F., Scaillet, B., Pichavant, M., Chiodini, G., 2009. Role of non-mantle CO_2 in the dynamics of volcano degassing: the Mount Vesuvius example. Geology 37, 319–322. https://doi.org/10.1130/G25446A.1.

Iacono-Marziano, G., Morizet, Y., Le Trong, E., Gaillard, F., 2012. New experimental data and semi-empirical parameterization of H_2O-CO_2 solubility in mafic melts. Geochim. Cosmochim. Acta 97, 1–23. https://doi.org/10.1016/j.gca.2012.08.035.

Johnston, F.K.B., Turchyn, A.V., Edmonds, M., 2011. Decarbonation efficiency in subduction zones: implications for warm Cretaceous climates. Earth Planet. Sci. Lett. 303, 143–152. https://doi.org/10.1016/j.epsl.2010.12.049.

Jolis, E.M., Freda, C., Troll, V.R., Deegan, F.M., Blythe, L.S., McLeod, C.L., Davidson, J.P., 2013. Experimental simulation of magma-carbonate interaction beneath Mt. Vesuvius, Italy. Contrib. Mineral. Petrol. 166, 1335–1353. https://doi.org/10.1007/s00410-013-0931-0.

Knuever, M., Sulpizio, R., Mele, D., Pisello, A., Costa, A., Perugini, D., Vetere, F., 2023. Decarbonation and clast dissolution timescales for short-term magma-carbonate interactions in the volcanic feeding system and their influence on eruptive dynamics: insights from experiments at atmospheric pressure. Chem. Geol. 639, 121724. https://doi.org/10.1016/j.chemgeo.2023.121724.

Konschak, A., Keppler, H., 2014. The speciation of carbon dioxide in silicate melts. Contrib. Mineral. Petrol. 167, 1–13. https://doi.org/10.1007/s00410-014-0998-2.

Lee, C.T.A., Shen, B., Slotnick, B.S., Liao, K., Dickens, G.R., Yokoyama, Y., Lenardic, A., Dasgupta, R., Jellinek, M., Lackey, J.S., Schneider, T., Tice, M.M., 2013. Continental arc-island arc fluctuations, growth of crustal carbonates, and long-term climate change. Geosphere 9, 21–36. https://doi.org/10.1130/GES00822.1.

Lee, C.-T.A., Jiang, H., Dasgupta, R., Torres, M., 2019. A Framework for understanding whole-Earth carbon cycling. In: Orcutt, B., Daniel, I., Dasgupta, R. (Eds.), Deep Carbon: Past to Present. Cambridge University Press, pp. 313–357.

Lustrino, M., Luciani, N., Stagno, V., Narzisi, S., Masotta, M., Scarlato, P., 2022. Experimental evidence on the origin of Ca-rich carbonated melts formed by interaction between sedimentary limestones and mantle-derived ultrabasic magmas. Geology 50, 476–480. https://doi.org/10.1130/G49621.1.

Mason, E., Edmonds, M., Turchyn, A.V., 2017. Remobilization of crustal carbon my dominate volcanic arc emissions. Science 357, 290–294.

Mollo, S., Gaeta, M., Freda, C., Di Rocco, T., Misiti, V., Scarlato, P., 2010. Carbonate assimilation in magmas: a reappraisal based on experimental petrology. Lithos 114, 503–514. https://doi.org/10.1016/j.lithos.2009.10.013.

Morris, R., Canil, D., 2022. CO_2 transport at shallow depths in arc magmas: evidence from unique orbicular dikes in the Jurassic Bonanza arc, Vancouver Island, Canada. Contrib. Mineral. Petrol. 177, 1–20. https://doi.org/10.1007/s00410-021-01852-y.

Ni, H., Keppler, H., 2013. Carbon in silicate melts. Rev. Mineral. Geochem. 75, 251–287. https://doi.org/10.2138/rmg.2013.75.9.

Papale, P., Moretti, R., Barbato, D., 2006. The compositional dependence of the saturation surface of H_2O + CO_2 fluids in silicate melts. Chem. Geol. 229, 78–95. https://doi.org/10.1016/j.chemgeo.2006.01.013.

Plank, T., Manning, C.E., 2019. Subducting carbon. Nature 574, 343–352. https://doi.org/10.1038/s41586-019-1643-z.

Ramos, E.J., Lackey, J.S., Barnes, J.D., Fulton, A.A., 2020. Remnants and rates of metamorphic decarbonation in continental arcs. GSA Today 30, 4–10. https://doi.org/10.1130/GSATG432A.1.

Shishkina, T., Botcharnikov, R.E., Holtz, F., Almeev, R.R., Portnyagin, M.V., 2010. Solubility of H_2O- and CO_2-bearing fluids in tholeiitic basalts at pressures up to 500 MPa. Chem. Geol. 277, 115–125. https://doi.org/10.1016/j.chemgeo.2010.07.014.

Spandler, C., Martin, L.H.J., Pettke, T., 2012. Carbonate assimilation during magma evolution at Nisyros (Greece), South Aegean Arc: evidence from clinopyroxenite xenoliths. Lithos 146–147, 18–33. https://doi.org/10.1016/j.lithos.2012.04.029.

Stolper, E., Epstein, S., 1991. An experimental study of oxygen isotope partitioning between silica glass and CO_2 vapor. In: Taylor Jr., H.P., O'Neill, J.R., Kaplan, I.R. (Eds.), Stable Isotope Geochemistry: A Tribute to Samuel Epstein, Geochemical Society Special Publication, vol. 3, pp. 35–51.

Troll, V.R., Deegan, F.M., 2023. The magma plumbing system of Merapi: The petrological perspective. In: Gertisser, R., et al. (Eds.), Merapi Volcano, Active Volcanoes of the World. Springer, pp. 233–263. https://doi.org/10.1007/978-3-031-15040-1_8.

Troll, V.R., Hilton, D.R., Jolis, E.M., Chadwick, J.P., Blythe, L.S., Deegan, F.M., Schwarzkopf, L.M., Zimmer, M., 2012. Crustal CO_2 liberation during the 2006 eruption and earthquake events at Merapi volcano, Indonesia. Geophys. Res. Lett. 39, 1–6. https://doi.org/10.1029/2012GL051307.

Troll, V.R., Deegan, F.M., Jolis, E.M., Harris, C., Chadwick, J.P., Gertisser, R., Schwarzkopf, L.M., Borisova, A.Y., Bindeman, I.N., Sumarti, S., Preece, K., 2013. Magmatic differentiation processes at Merapi Volcano: inclusion petrology and oxygen isotopes. J. Volcanol. Geotherm. Res. 261, 38–49. https://doi.org/10.1016/j.jvolgeores.2012.11.001.

Weis, F.A., Skogby, H., Troll, V.R., Deegan, F.M., Dahren, B., 2015. Magmatic water contents determined through clinopyroxene: examples from the Western Canary Islands, Spain. Geochem. Geophys. Geosyst. 16, 2127–2146. https://doi.org/10.1002/2015GC005800.

Weis, F.A., Stalder, R., Skogby, H., 2016. Experimental hydration of natural volcanic clinopyroxene phenocrysts under hydrothermal pressures (0.5-3 kbar). Am. Mineral. 101, 2233–2247. https://doi.org/10.2138/am-2016-5711CCBYNCND.

Whitley, S., Gertisser, R., Halama, R., Preece, K., Troll, V.R., Deegan, F.M., 2019. Crustal CO_2 contribution to subduction zone degassing recorded through calc-silicate xenoliths in arc lavas. Sci. Rep. 9, 1–11. https://doi.org/10.1038/s41598-019-44929-2.

Whitley, S., Halama, R., Gertisser, R., Preece, K., Deegan, F.M., Troll, V.R., 2020. Magmatic and metasomatic effects of magma–carbonate interaction recorded in calc-silicate xenoliths from Merapi volcano (Indonesia). J. Petrol. 61, 1–38. https://doi.org/10.1093/petrology/egaa048.